Springer

Acta Mechanica Sinica

CrossMark click for updates

• RESEARCH PAPER •

Acta Mech. Sin., Vol. 39, 722306 (2023)
https://doi.org/10.1007/s10409-022-22306-x

# Virtual element formulation for gradient elasticity

Peter Wriggers*, and Blaž Hudobivnik*

*Institute for Continuum Mechanics, Leibniz Universität Hannover, Hannover, Germany*

Received August 12, 2022; accepted October 14, 2022; published online February 13, 2023

The virtual element method has been developed over the last decade and applied to problems in solid mechanics. Different formulations have been used regarding the order of ansatz, stabilization of the method and applied to a wide range of problems including elastic and inelastic materials and fracturing processes. This paper is concerned with formulations of virtual elements for higher gradient elastic theories of solids using the possibility, inherent in virtual element methods, of formulating $C^1$-continuous ansatz functions in a simple and efficient way.

**Virtual element method, Gradient elasticity, $C^1$-continuity**

**Citation:** P. Wriggers, and B. Hudobivnik, Virtual element formulation for gradient elasticity, Acta Mech. Sin. **39**, 722306 (2023), https://doi.org/10.1007/s10409-022-22306-x

## 1. Introduction

Modeling of materials displaying size effects has attracted ongoing attention. Size effects have been observed in the response of materials by Bažant [1], for concrete, [2] for metals and in Ref. [3] for metal composites. Size effects can be related to microstructural behaviour and are observed for specimen of a small size that is of the order of the microstructure. At this length scale, specimens with similar shape but different dimensions depict different mechanical behavior [4]. Within the classical continuum theory these size effects cannot be captured, since internal length scales are negelected. Hence an extension of standard continuum mechanics is required.

Extensions of the classical continuum theory are more than hundred years old. Additional rotational degrees of freedom were introduced at the micro level and can be found in Ref. [5] which is now frequently used in shell theories. The potential of such generalization was discussed in the contribution by Hellinger [6], but there was no follow up work until in the early sixties. At that time scientists became interested in the continuum description of generalized and higher order theories [7-12].

The theoretical formulations of gradient theories are based on the introduction of higher order gradients that lead to boundary value problems which require higher continuites within discretization schemes used in numerical simulations. The higher order gradient elasticity theory leads to a weak form which can only be discretized consistently with $C^1$-continuous ansatz functions. In this paper we aim at using the advantage of the virtual element method to derive higher order ansatz functions which are $C^1$-continuous. Hence the virtual element method can be directly applied to a special class of problems related to strain gradient elasticity when the micro deformation coincides with the gradient of macroscopic displacements, see also Ref. [10].

In the theory of gradient elasticity, the strain energy is a function as well of the strain as of its derivative [13]. Consequently, classical stress measures and higher order ones have to be introduced that depend on higher-order derivatives of the displacements. Since the aim of this contribution is to demonstrate that the virtual element method can be efficiently employed to solve such problems, we restrict the

*Corresponding authors. E-mail addresses: wriggers@ikm.uni-hannover.de (Peter Wriggers); hudobivnik@ikm.uni-hannover.de (Blaž Hudobivnik)
Executive Editor: Juan Ma

theoretical framework to the simplest possible formulation of strain gradient elasticity [14]. In this work the strains and derivatives of the strain are introduced together with one additional material parameter, which describes the internal material length scale. It was shown in Ref. [15] that this specific gradient elasticity theory models size effects in a sufficient way. The results related to the theoretical model were proven by experiments [16], and also the recent survey in Ref. [17]. Extensions of gradient theories to finite strain problems can be found [18, 19].

Numerical models that treat the strain gradient theory for elasticity can be found [20-23], which employed special finite elements. In Ref. [24], a new method was applied to higher order parial differntial equations that combined concepts from the continuous Galerkin method, the discontinuous Galerkin method and stabilization techniques. Among other applications, it was used to treat strain gradient elasticity. Further applications of strain gradient elasticity can be found by Lesičar et al. [25], who applied the theory within a two-scale description of solids. Strain gradient elasticity was also treated in beam theories [26, 27]. In Ref. [28], special natural and finite element discretizations are compared and applied to higher order continua. Furthermore, Fischer et al. [29] employed an isogeometrical formulation of strain gradient theories which allows the construction of $C^1$-continuous discretizations. A concise treatment of different approaches including also $C^1$-continuous Hermitian ansatz spaces can be found in Ref. [30].

The development of virtual elements for problems in elasticity started with Refs. [31-33]. Other applications in the engineering range can be found for nonlinear elasticity in Refs. [34,35], contact mechanics in Ref. [36] and phase field methods for fracture in Ref. [37] among others.

In case of higher order virtual element formulations, basic work regarding $C^n$-continuous ansatz functions was firstly described in Ref. [38] who treated Kirchhoff plates. Further work in this direction can be found in Refs. [39-43]. Other formulations using $C^1$-continuous virtual elements are dedicated to Cahn-Hillard equations [44], and to general biharmonic equations [45]. The basic ideas which lead to the virtual element ansatz functions for a Kirchhoff plate can be applied to strain gradient elasticity. However, here two displacement components have to be considered and rotations are nonexistent. In this contribution, we will provide a virtual element formulation for geometrically linear and finite deformation responses in gradient elasticity. After a short review of the underlying continuum mechanics formulation, we will provide details of the virtual element formulation. Examples demonstrate the applicability and good approximation properties of the new virtual element scheme.

## 2. Continuum equations for higher order elasticity

Consider an elastic body that occupies the bounded domain $\Omega \subset \mathbb{R}^2$. The body $\Omega$ has a boundary $\Gamma$ which comprises non-overlapping sections $\Gamma_D$ and $\Gamma_N$ such that $\Gamma_D \cup \Gamma_N = \Gamma$ (Fig. 1).

The position $\mathbf{x}$ of a material point initially at $\mathbf{X}$ is given by the motion

$$\mathbf{x} = \boldsymbol{\varphi}(\mathbf{X}, t) = \mathbf{X} + \mathbf{u}(\mathbf{X}, t), \tag{1}$$

where $\mathbf{u}(\mathbf{X}, t)$ is the displacement. We also define the deformation gradient $\mathbf{F}$ by

$$\mathbf{F}(\mathbf{X}, t) = \mathrm{Grad}\, \boldsymbol{\varphi}(\mathbf{X}, t) = \nabla_X \boldsymbol{\varphi}(\mathbf{X}, t) = \mathbf{1} + \nabla_X \mathbf{u}(\mathbf{X}, t), \tag{2}$$

the gradient being evaluated with respect to $\mathbf{X}$.

As a measure for the homogeneity of the strain, the strain gradient is defined as the gradient of $\mathbf{F}$:

$$\mathbf{G}(\mathbf{X}, t) = \mathrm{Grad}\, \mathbf{F}(\mathbf{X}, t) = \nabla_X^2 \boldsymbol{\varphi}(\mathbf{X}, t) = \nabla_X^2 \mathbf{u}(\mathbf{X}, t), \tag{3}$$

with the components $[\nabla_X^2 \mathbf{u}]_{ijk} = u_{i,jk}$.

The internal potential energy is assumed to depend on the stored mechanical energy:

$$U_{\mathrm{int}} = \int_{\Omega} W(\mathbf{F}, \mathbf{G})\, \mathrm{d}\Omega, \tag{4}$$

where the strain energy $W(\mathbf{F}, \mathbf{G})$ is now a function of the deformation gradient and the strain gradient. The external energy can be formulated for the volume and surface loads as

$$U_{\mathrm{ext}} = -\int_{\Omega} \bar{\mathbf{b}} \cdot \boldsymbol{\varphi}\, \mathrm{d}\Omega - \int_{\Gamma_N} \bar{\mathbf{t}}^1 \cdot \boldsymbol{\varphi}\, \mathrm{d}\Gamma - \int_{\Gamma_N} \bar{\mathbf{t}}^2 \cdot \nabla_X^N \boldsymbol{\varphi}\, \mathrm{d}\Gamma, \tag{5}$$

where the volume load $\bar{\mathbf{b}}$ and the traction load $\bar{\mathbf{t}}^1$ are defined in Fig. 1. In Eq. (5), the projection of the derivative

$$\begin{aligned} \nabla_X(\bullet) &= [\mathbf{1} - \mathbf{N} \otimes \mathbf{N}] \cdot \nabla_X(\bullet) + \nabla_X(\bullet) \cdot [\mathbf{N} \otimes \mathbf{N}] \\ &= \nabla_X^S(\bullet) + \nabla_X^N(\bullet) \otimes \mathbf{N}, \end{aligned} \tag{6}$$

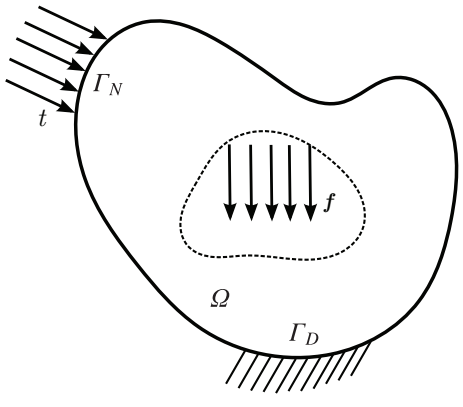


**Figure 1** Solid with boundary conditions.

onto a tangential and normal direction was used where $\nabla_X^N = \nabla_X(\bullet)\cdot\mathbf{N}$.

The internal and external part of the energy yields the total potential:

$$U = U_{\text{int}} + U_{\text{ext}}, \tag{7}$$

which is basis for the derivative of the virtual element.

Variation of the internal potential yields

$$\delta U_{\text{int}} = \int_\Omega \frac{\partial W(\mathbf{F},\mathbf{G})}{\partial \mathbf{F}} : \delta\mathbf{F} + \frac{\partial W(\mathbf{F},\mathbf{G})}{\partial \mathbf{G}} \vdots \delta\mathbf{G}\, \mathrm{d}\Omega, \tag{8}$$

where

$$\mathbf{P} = \frac{\partial W(\mathbf{F},\mathbf{G})}{\partial \mathbf{F}} \tag{9}$$

is the first Piola-Kirchhoff stress tensor, and

$$\mathbf{Q} = \frac{\partial W(\mathbf{F},\mathbf{G})}{\partial \mathbf{G}} \tag{10}$$

is the double stress. This leads to the stress divergence term for gradient elasticity

$$\begin{aligned}\delta U_{\text{int}} &= \int_\Omega \mathbf{P} : \delta\mathbf{F} + \mathbf{Q} \vdots \delta\mathbf{G}\, \mathrm{d}\Omega \\ &= \int_\Omega P_{ik}\,\delta F_{ik} + Q_{ijk}\,\delta G_{ijk}\, \mathrm{d}\Omega\,.\end{aligned} \tag{11}$$

The Dirichlet and Neumann boundary conditions are formulated for the first order $()^1$ and second order terms $()^2$, respectively:

$$\begin{aligned}
&\mathbf{u} = \bar{\mathbf{u}}, && \text{on } \Gamma_D^1,\\
&\nabla_X^N\boldsymbol{\varphi} = \nabla_X^N\bar{\boldsymbol{\varphi}}, && \text{on } \Gamma_D^2,\\
&[\mathbf{P} - \nabla_X\cdot\mathbf{Q}]\cdot\mathbf{N} + [\nabla_X^S\cdot\mathbf{N}]\mathbf{Q} : [\mathbf{N}\otimes\mathbf{N}] && \\
&\quad - \nabla_X^S\cdot[\mathbf{Q}\cdot\mathbf{N}]^{\mathrm{T}} = \bar{\mathbf{t}}^1, && \text{on } \Gamma_N^1,\\
&\mathbf{Q} : [\mathbf{N}\otimes\mathbf{N}] = \bar{\mathbf{t}}^2, && \text{on } \Gamma_N^2,
\end{aligned} \tag{12}$$

with $\mathbf{N}$ the outward unit normal vector and using Eq. (6). The prescribed displacement $\bar{\mathbf{u}}$ and the prescribed gradient $\nabla_X^N\bar{\boldsymbol{\varphi}}$ are acting on the surfaces $\Gamma_D^1$ and $\Gamma_D^2$. The prescribed surface traction $\bar{\mathbf{t}}^1$ and the prescribed double stresses $\bar{\mathbf{t}}^2$ are related to the surfaces $\Gamma_N^1$ and $\Gamma_N^2$, respectively. Note that one recovers for constant $\mathbf{Q}$ and $\mathbf{N}$ the classical Neuman boundary condition $\mathbf{P}\cdot\mathbf{N} = \bar{\mathbf{t}}^1$ on $\Gamma_N^1$.

Generally the strain energy is constructed using an additive split:

$$W(\mathbf{F},\mathbf{G}) = W^1(\mathbf{F}) + W^2(\mathbf{G}), \tag{13}$$

where for the classical strain energy $W^1(\mathbf{F})$ a homogeneous compressible isotropic hyperelastic material is formulated. The simplest choice is a neo-Hookean strain energy function. This yields for the two-dimensional (2D) case:

$$W^1(\mathbf{F}) = \frac{\lambda}{4}(J^2 - 1 - 2\ln J) + \frac{\mu}{2}(\mathbf{F}:\mathbf{F} - 2 - 2\ln J), \tag{14}$$

where $\lambda$ and $\mu$ are the Lamé constants. The Jacobian $J$ of the deformation is given as $J = \det\mathbf{F}$. This leads to

$$\mathbf{P} = \frac{\partial W^1(\mathbf{F})}{\partial \mathbf{F}} = \frac{\lambda}{2}(J-1)\mathbf{F}^{-\mathrm{T}} + \mu\,(\mathbf{F} - \mathbf{F}^{-\mathrm{T}})\,. \tag{15}$$

The simplest choice for the part $W^2(\mathbf{G})$ is given by

$$\begin{aligned}
W^2(\mathbf{G}) &= \mu\, l^2\,\mathbf{G}\vdots\mathbf{G} + \frac{\lambda}{2} l^2\,(\mathbf{1}:\mathbf{G})\cdot(\mathbf{1}:\mathbf{G}),\\
W^2(G_{ijk}) &= \mu\, l^2\, G_{ijk}G_{ijk} + \frac{\lambda}{2} l^2\, G_{jji}\,G_{kki}\,,
\end{aligned} \tag{16}$$

with the second order unit tensor $\mathbf{1}$. Here $l$ is a length scale that governs the influence of the part $W^2$ within the model for the strain gradient elasticity. It has to be determined from experimental observations. Equation (16) yields the double stress:

$$\mathbf{Q} = \frac{\partial W^2(\mathbf{G})}{\partial \mathbf{G}} = \mu\, l^2\,\mathbf{G} + \lambda\, l^2\,\mathbb{I} : \mathbf{G}, \tag{17}$$

where $\mathbb{I}$ is the fourth order unit tensor which maps a second order tensor onto itself $A_{ij} = \mathbb{I}_{ijlm}A_{lm}$. Often the second term will be neglected in Eq. (16) which then simplifies the strain energy and double stress to

$$\begin{aligned}
&W^2(\mathbf{G}) = \mu\, l^2\,\mathbf{G}\vdots\mathbf{G} \iff W^2(G_{ijk}) = \mu\, l^2\, G_{ijk}G_{ijk},\\
&\mathbf{Q} = \mu\, l^2\,\mathbf{G} \qquad\quad \iff Q_{ijk} = \mu\, l^2\, G_{ijk}\,.
\end{aligned} \tag{18}$$

In case of a kinematically linear gradient theory the strain energy $W^1$ can be expressed by the strain tensor, being the symmetric part of the displacement gradient:

$$\boldsymbol{\varepsilon} = \frac{1}{2}(\nabla_X\mathbf{u} + \nabla_X^{\mathrm{T}}\mathbf{u}), \tag{19}$$

with the index notation $\varepsilon_{ij} = \frac{1}{2}(u_{i,j} + u_{j,i})$. The second part of the strain energy $W^2$ is given in terms of the strain gradient $\boldsymbol{\gamma}$, being the gradient of the strain tensor:

$$\boldsymbol{\gamma} = \nabla_X\boldsymbol{\varepsilon}, \quad \text{with } \gamma_{ijk} = \varepsilon_{jk,i} = \frac{1}{2}(u_{j,ki} + u_{k,ji}). \tag{20}$$

The strain energy is now given by the linearization of Eqs. (14) and (16) as

$$W(\boldsymbol{\varepsilon},\boldsymbol{\gamma}) = \frac{1}{2}\lambda(\varepsilon_{ii}\,\varepsilon_{jj} + l^2\,\gamma_{jji}\,\gamma_{kki}) + \mu\,(\varepsilon_{ij}\varepsilon_{ij} + l^2\,\gamma_{ijk}\,\gamma_{ijk}), \tag{21}$$

which can be written in direct notation as

$$\begin{aligned}
W(\boldsymbol{\varepsilon},\boldsymbol{\gamma}) = \frac{1}{2}\lambda\Big[\,[\mathrm{tr}\,\boldsymbol{\varepsilon}]^2 + l^2\,(\mathbf{1}:\nabla_X\boldsymbol{\varepsilon})\cdot(\mathbf{1}:\nabla_X\boldsymbol{\varepsilon})\Big]\\
+ \mu\,(\boldsymbol{\varepsilon}:\boldsymbol{\varepsilon} + l^2\nabla_X\boldsymbol{\varepsilon}\vdots\nabla_X\boldsymbol{\varepsilon}).
\end{aligned} \tag{22}$$

## 3. Development of the ansatz for the virtual element based on strain gradient theory

Due to the appearance of the gradient of the deformation gradient $\mathbf{G} = \nabla_X \mathbf{F}$ in the potential energy (4), also the strain energy (13), it is necessary to employ a $C^1$-continuous ansatz within the discretization.

### 3.1 Ansatz function

In this section we will provide ansatz functions for 2D gradient elasticity. A $C^1$-continous formulation can be found for virtual plate elements, in e.g., Refs. [39,46], for Cahn-Hillard equations in Ref. [44] and for general biharmonic equations in Ref. [45]. The procedure, to derive the ansatz functions for the virtual element method, is provided next.

Since elements for the strain gradient elasticity need a $C^1$-continuous ansatz, the following space for an ansatz of order $n$ is introduced:

$$V_{h|\Omega_v} = \{\mathbf{u}_h \in [H^2(\Omega_v)]^2, \Delta^2 \mathbf{u}_h \in P_{n-4}(\Omega_v), \\ \mathbf{u}_{h,t} \in P_r(\Gamma_e), \mathbf{u}_{h,n} \in P_s(\Gamma_e)\}, \tag{23}$$

where we set $P_{n-4}(\Omega_v) = \{0\}$ for $n < 4$. The parameters $r$ and $s$ describe the ansatz order for the derivatives in normal and tangent direction $\mathbf{u}_{h,t}$ and $\mathbf{u}_{h,n}$, respectively, and can be chosen differently. The condition $\Delta^2 \mathbf{u} \in P_{n-4}(\Omega_v)$ is fundamental for the element to be uni-solvent which ensures the uniqueness of the displacement $\mathbf{u}$ inside the element.
With this definition it is straight forward to design virtual shell elements that fulfill $C^1$-continuity, note that the ansatz for $\mathbf{u}_h$ has only to be formulated at the boundary.

The ansatz function for the displacement $\mathbf{u}_h$ has to be formulated in two dimensions. It has the properties:

(1) $\mathbf{u}_h$ , $\mathbf{u}_{h,t}$ and $\mathbf{u}_{h,n}$ are known at the vertices $k$ of the polygon $\Omega_v$;

(2) $\mathbf{u}_h$ is a polynomial $\mathrm{P}_n$ of degree $n$ at each edge $\Gamma_e \in \Gamma_v$;

(3) $\mathbf{u}_{h,t}$ is a polynomial $\mathrm{P}_r$ of degree $r = n - 1$ at each edge $\Gamma_e \in \Gamma_v$;

(4) $\mathbf{u}_{h,n}$ is a polynomial $\mathrm{P}_s$ of degree $s$ at each edge $\Gamma_e \in \Gamma_v$ with additional unknowns of $\mathbf{u}_{h,n}$ at $s - 1$ equally spaced points at $\Gamma_e$;

(5) $\mathbf{u}_h$ , $\mathbf{u}_{h,t}$ and $\mathbf{u}_{h,n}$ are continuous at all edges $\Gamma_e \in \Gamma_v$ of the polygon $\Omega_v$;

(6) $\Delta^2 \mathbf{u}_h$ is a polynomial of degree $\mathrm{P}_{n-4}$ on the polygon $\Omega_v$.

With these definitions the ansatz for the displacement $\mathbf{u}_h$ is a harmonic function inside $\Omega_v$ which is only known at the edges $\Gamma_e$ of $\Omega_v$ with $\Gamma_v = \cup \Gamma_e$.

To connect the ansatz defined in (1) to (6) to the strains and strain gradients in the virtual element $\Omega_e$ a special projection onto the polynomial ansatz space $\mathbf{u}_h \mapsto \Pi(\mathbf{u}_h) = \mathbf{u}_\pi$ is employed. In this paper we construct two elements that use a polynomial $\mathbf{N}_\pi^n$ of the ansatz order $n = 2$ and $n = 3$. The projection is denoted by

$$\mathbf{u}_\pi = \begin{Bmatrix} [u_\pi]_1 \\ [u_\pi]_2 \end{Bmatrix} = \mathbf{a}\, \mathbf{N}_\pi^n, \quad \text{with } [u_\pi]_i = \mathbf{a}_i\, \mathbf{N}_\pi^n, \tag{24}$$

with the constants $\mathbf{a}_i = \{a_{i1}, a_{i2}, a_{i3}, \ldots, a_{ip}\}$ for each of the components of $[u_\pi]_i$. Note that $p = 6$ for an a quadratic ansatz with $(n = 2)$ and $p = 10$ for a cubic ansatz $(n = 3)$. In index notation we can write $[u_\pi]_i = a_{ip}\, [N_\pi^n]_p$.

Additionally $\mathbf{w} = \mathbf{a}^w\, \mathbf{N}_\pi^n$ is introduced which has the role of a test function where $\mathbf{a}_i^w = \{a_{i1}^w, a_{i2}^w, a_{i3}^w, \ldots, a_{ip}^w\}$ are the $p = 6/10$ parameters for each of the components $w_i$ of the test function $\mathbf{w}$ for elements 1 and 2, respectively.

The projection $\mathbf{u}_h \mapsto \Pi(\mathbf{u}_h) = \mathbf{u}_\pi$ is based on the orthogonal projection of the strain gradient $\nabla\nabla \mathbf{u}_h$:

$$\int_{\Omega_v} (\nabla\nabla \mathbf{u}_h - \nabla\nabla \mathbf{u}_\pi) \vdots \nabla\nabla \mathbf{w}\, \mathrm{d}\Omega = 0, \tag{25}$$

which can be written in index notation as

$$\int_{\Omega_v} [u_\pi]_{i,jk}\, w_{i,jk}\, \mathrm{d}\Omega = \int_{\Omega_v} [u_h]_{i,jk}\, w_{i,jk}\, \mathrm{d}\Omega. \tag{26}$$

This equation is accompanied for the computation of the constant and linear terms in the ansatz (24) by the equality of mean displacements:

$$\int_{\Gamma_v} \mathbf{u}_\pi\, \mathrm{d}\Gamma = \int_{\Gamma_v} \mathbf{u}_h\, \mathrm{d}\Gamma \iff \int_{\Gamma_v} [u_\pi]_i\, \mathrm{d}\Gamma = \int_{\Gamma_v} [u_h]_i\, \mathrm{d}\Gamma, \tag{27}$$

and the equality of the mean gradients:

$$\int_{\Omega_v} \nabla \mathbf{u}_\pi\, \mathrm{d}\Omega = \int_{\Omega_v} \nabla \mathbf{u}_h\, \mathrm{d}\Omega \\ \iff \int_{\Omega_v} [u_\pi]_{i,j}\, \mathrm{d}\Gamma = \int_{\Gamma_v} [u_h]_i\, n_j\, \mathrm{d}\Gamma, \tag{28}$$

where $n_j$ are the components of the outward normal vector at the element boundary.

A quadratic and a cubic polynomial are selected for $\mathbf{N}_\pi^n$ to approximate the deflection $[u_\pi]_i$. They produce a constant $(n = 2)$ and linear strain gradient $(n = 3)$:

$$\mathbf{N}_\pi^2 = (1, X, Y, X^2, XY, Y^2), \quad \text{for } n{=}\ 2, \tag{29}$$

$$\mathbf{N}_\pi^3 = (1, X, Y, X^2, XY, Y^2, X^3, X^2Y, XY^2, Y^3), \text{ for } n{=}\ 3. \tag{30}$$

In Fig. 2, the virtual element for the ansatz $(n = 3)$ is depicted with the nodal degrees of freedom at the edge $e$:

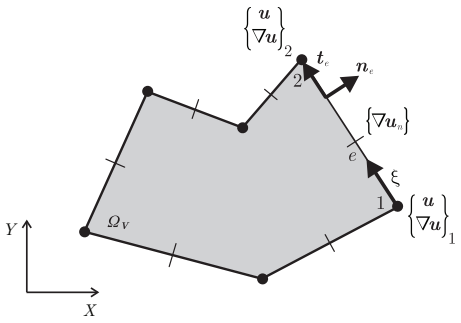


**Figure 2** Virtual element for linear strain ($n = 3$).

$$\mathbf{u}_e = \begin{Bmatrix} \mathbf{u}_1 \\ \mathbf{u}_2 \end{Bmatrix} = \begin{Bmatrix} u_1 \\ v_1 \\ u_2 \\ v_2 \end{Bmatrix}, \quad \text{and} \quad \nabla\mathbf{u}_e = \begin{Bmatrix} \mathbf{u}_{1,X} \\ \mathbf{u}_{1,Y} \\ \mathbf{u}_{2,X} \\ \mathbf{u}_{2,Y} \end{Bmatrix}, \tag{31}$$

and the normal derivatives $\mathbf{u}_{m,n} = \{u_{,n}\ ,\ v_{,n}\}$ at the midpoints of the edge. This amounts to six degrees of freedom per node and additional two degrees of freedom per edge. In case of the ansatz ($n = 2$), the nodal degrees at the mid points of the edge will not be used.

To ensure the $C^1$ continuity requirement of the ansatz functions, the values of $u_i$ and its derivatives in normal, $u_{i,n}$, and tangential, $u_{i,t}$, direction have to match along the edge between two adjacent elements. The following relations hold for the derivatives in normal and tangential direction for the component of $u_i$:

$$\begin{aligned} &\nabla u_i \cdot \mathbf{t}_e = u_{i,t}, \quad \text{and} \quad \nabla v_i \cdot \mathbf{t}_e = v_{i,t}, \\ &\nabla u_i \cdot \mathbf{n}_e = u_{i,n}, \quad \text{and} \quad \nabla v_i \cdot \mathbf{n}_e = v_{i,n}\,. \end{aligned} \tag{32}$$

In the 2D case, normal and tangent vectors are given for a segment $e$ as

$$\begin{aligned} \mathbf{n}_e &= \begin{Bmatrix} n_X \\ n_Y \end{Bmatrix}_e = \frac{1}{l_e} \begin{Bmatrix} -(Y_2^r - Y_1^r) \\ X_2^r - X_1^r \end{Bmatrix}_w \\ \text{and } \mathbf{t}_e &= \begin{Bmatrix} t_X \\ t_Y \end{Bmatrix}_e = \frac{1}{l_e} \begin{Bmatrix} X_2^r - X_1^r \\ Y_2^r - Y_1^r \end{Bmatrix}_e , \end{aligned} \tag{33}$$

where $l_e$ is the length of the segment $e$ and $(X_i^r\,, Y_i^r)$ with $i = \{1, 2\}$ are the nodes of the vertices defining the segment.

Now the derivatives in normal and tangential direction at an edge $\Gamma_e$ can be written as

$$\mathbf{u}_{i,n} = \begin{Bmatrix} u_{i,n} \\ v_{i,n} \end{Bmatrix} \quad \text{and} \quad \mathbf{u}_{i,t} = \begin{Bmatrix} u_{i,t} \\ v_{i,t} \end{Bmatrix}, \tag{34}$$

where $i = 1, 2$ denotes the node at the edge.

A cubic Hermitian ansatz for the displacement $\mathbf{u}_h$ is selected at the element edge $\Gamma_e$ for both element types:

$$(\mathbf{u}_h)_e = H_1(\xi_e)\,\mathbf{u}_1 + l_e H_1'(\xi_e)\,\mathbf{u}_{1,t} + H_2(\xi_e)\,\mathbf{u}_2 + l_e H_2'(\xi_e)\,\mathbf{u}_{2,t}, \tag{35}$$

where the basis functions are defined in terms of Hermite splines:

$$\begin{aligned} &H_1(\xi_e) = 2\xi_e^3 - 3\xi_e^2 + 1, \ H_1'(\xi_e) = \xi_e^3 - 2\xi_e^2 + \xi_e, \\ &H_2(\xi_e) = -2\xi_e^3 + 3\xi_e^2, \quad H_2'(\xi_e) = \xi_e^3 - \xi_e^2. \end{aligned} \tag{36}$$

The differentiation in tangential direction $\mathbf{u}_{,t}$ in Eq. (32) is then obtained by the scaled derivative of Eq. (36) with respect to the local coordinate $\xi_e$ at the element edge $\Gamma_e$:

$$(\mathbf{u}_{,t})_e = \frac{1}{l_e} \frac{\mathrm{d}(\mathbf{u}_h)_e}{\mathrm{d}\xi_e}, \tag{37}$$

which has the explicit form

$$\begin{aligned} (\mathbf{u}_{,t})_e &= \frac{6}{l_e}(\xi_e^2 - \xi_e), \mathbf{u}_1 + (3\xi_e^2 - 4\xi_e + 1)\,\mathbf{u}_{1,t} \\ &\quad + \frac{6}{l_e}(-\xi_e^2 + \xi_e), \mathbf{u}_2 + (3\xi_e^2 - 2\xi_e)\,\mathbf{u}_{2,t} \end{aligned} \tag{38}$$

for both elements.

The normal derivative $\mathbf{u}_{,n}$ at the edge $\Gamma_e$ is defined by a linear ansatz for element 1 and a quadratic ansatz for element 2:

$$(\mathbf{u}_{,n})_e = (1 - \xi_e)\,\mathbf{u}_{1,n} + \xi_e\,\mathbf{u}_{2,n}, \text{ for element 1,} \tag{39}$$

$$\begin{aligned} (\mathbf{u}_{,n})_e &= (2\xi_e^2 - 3\xi_e + 1)\,\mathbf{u}_{1,n} + (2\xi_e^2 - 1)\,\mathbf{u}_{2,n} \\ &\quad + 4(\xi_e - \xi_e^2)\,\mathbf{u}_{m,n}, \text{ for element 2.} \end{aligned} \tag{40}$$

This results to one additional unknown $\mathbf{u}_{m,n}$ for the quadratic ansatz of element 2 at the mid point of the edge, as demonstrated in Fig. 2.

Before inserting the ansatz function (35), (39) and (40) into the right hand side of the projection (26) and the equivalence of the mean values for the displacement (27) and the gradient (28), one has to relate the derivatives $(u_{i,n}, u_{i,t})$ to the global derivatives $(u_{i,X}, u_{i,Y})$. This follows from the transformation:

$$\begin{Bmatrix} u_{i,X} \\ u_{i,Y} \end{Bmatrix} = \begin{bmatrix} n_X & t_X \\ n_Y & t_Y \end{bmatrix}^{\mathrm{T}} \begin{Bmatrix} u_{i,n} \\ u_{i,t} \end{Bmatrix} \quad \text{and} \quad \begin{Bmatrix} v_{i,X} \\ v_{i,Y} \end{Bmatrix} = \begin{bmatrix} n_X & t_X \\ n_Y & t_Y \end{bmatrix}^{\mathrm{T}} \begin{Bmatrix} v_{i,n} \\ v_{i,t} \end{Bmatrix} \tag{41}$$

with the tangential and normal vectors $(\mathbf{t}_e, \mathbf{n}_e)$ that change from edge to edge of the virtual element.

The projection of the component $[u_\pi]_i$ of $\mathbf{u}_\pi = \{[u_\pi]_1, [u_\pi]_2\} = \{u_\pi, v_\pi\}$ is approximated like $w$ by $[u_\pi]_i = a_{ip}\,[N_\pi^n]_p$ leading to the strain gradient

$$[u_\pi]_{i,jk}^{(2)} = a_{ip}\,[N_\pi^2]_{p,jk} \text{ and } [u_\pi]_{i,jk}^{(3)} = a_{ip}\,[N_\pi^3]_{p,jk} \tag{42}$$

and the virtual strain gradient

$$w_{i,jk}^{(2)} = a_{ip}^w\,[N_\pi^2]_{p,jk} \text{ and } w_{i,jk}^{(3)} = a_{ip}^w\,[N_\pi^3]_{p,jk} \tag{43}$$

for the first end second virtual element, respectively. By combining (25), (27) and (28), we obtain for the right hand side:

$$g_b = \int_{\Gamma_v} a^w_{i1}\,[u_\pi]^{(n)}_i \,\mathrm{d}\Gamma + \int_{\Omega_v} \left[a^w_{i(j+1)}[u_\pi]^{(n)}_{i,j} + [u_\pi]^{(n)}_{i,jk}\, w^{(n)}_{i,jk}\right] \mathrm{d}\Omega$$

$$\Longrightarrow \mathbf{G}_b = \frac{\partial^2 g_b}{\partial \mathbf{a}^w \partial \mathbf{a}}. \tag{44}$$

An exact integration is possible for all integrals in $g_b$ since they only contain polynomials. It will lead to a matrix $\mathbf{G}_b$ that forms the equation system:

$$\mathbf{G}_b\,\mathbf{a} = \mathbf{b}_b, \tag{45}$$

where now only the right hand side has to be computed from integrating the right hand side in Eqs. (25) and (28) by parts [46]:

$$\begin{aligned}\int_{\Omega_v} [u_h]_{i,jk}\, w_{i,jk}\,\mathrm{d}\Omega = &\int_{\Gamma_v} w_{i,jk}\,[u_h]_{i,j}\, n_k \mathrm{d}\Gamma \\ &- \int_{\Gamma_v} w_{i,jkk}\,[u_h]_i\, n_j\,\mathrm{d}\Gamma \\ &+ \int_{\Omega_v} [u_h]_i\, w_{i,jjkk}\,\mathrm{d}\Omega\,.\end{aligned} \tag{46}$$

Note that the ansatz function for the test function $\mathbf{w}_h$ is of third order and thus the term $w_{i,jjkk}$ vanishes. Hence one obtains

$$\begin{aligned}b_b = &\sum_{e=1}^{n_e} \int_{\Gamma_e} \left(a^v_{i1} + a^w_{ij+1}\, n^e_i - w_{i,jkk}\, n^e_i\right) [u_h]_j \,\mathrm{d}\Gamma \\ &+ \int_{\Gamma_e} w_{i,jk}\,[u_h]_{i,j}\, n^e_k \,\mathrm{d}\Gamma\,.\end{aligned} \tag{47}$$

For the assumed straight edges of the element, the normal $\mathbf{n}_e$ is constant and furthermore $\mathrm{div}(\nabla\nabla v)$ is constant for $n = 3$ and even zero for a quadratic ansatz ($n = 2$). Hence Eq. (47) can be simplified as

$$\begin{aligned}b_b = &\sum_{e=1}^{n_e} \left[\left(a^w_{i1} + a^w_{ij+1}\, n^e_i - w_{i,jkk}\, n^e_i\right) \int_{\Gamma_e} [u_h]_j \,\mathrm{d}\Gamma \right. \\ &\left. + \int_{\Gamma_e} w_{i,jk}\,[u_h]_{i,j}\, n^e_k \,\mathrm{d}\Gamma\right].\end{aligned} \tag{48}$$

The derivative of this equation with respect to the parameters of the test function yields finally:

$$\mathbf{b}_b = \frac{\partial b_b}{\partial \mathbf{a}^w}, \tag{49}$$

which is required in Eq. (45). With the ansatz functions for $[u_h]_i$, provided in Eqs. (39) and (40), all integrations can be carried out in Eq. (48).

By using both ansatz functions for $[u_i]_h$, the projected ansatz $[u_i]_\pi$ can be deduced from Eqs. (24) and (45) for the two different elements. This yields a general mapping that defines the displacement field of the virtual element in terms of the nodal unknowns:

$$\mathbf{u}_\pi = \mathbb{B}_\beta(X, Y)\,\mathbf{U}_{e\beta}, \tag{50}$$

where $\beta = 1, 2$ stand for the different elements. In more detail, the nodal unknown vectors $\mathbf{u}_\beta$ of the two elements with $n_v$ vertices are given by

$$\begin{aligned}\mathbf{U}_{e1} &= \{\mathbf{u}_1, \mathbf{u}_{1,X}, \mathbf{u}_{1,Y}, \mathbf{u}_2, \mathbf{u}_{2,X}, \mathbf{u}_{2,Y} \ldots, \mathbf{u}_{n_v}, \mathbf{u}_{n_v,X}, \mathbf{u}_{n_v,Y}\}^{\mathrm{T}}, \\ \mathbf{U}_{e2} &= \{\mathbf{u}_1, \mathbf{u}_{1,X}, \mathbf{u}_{1,Y}, \mathbf{u}_{1\text{-}2,n}, \mathbf{u}_2, \mathbf{u}_{2,X}, \mathbf{u}_{2,Y}, \mathbf{u}_{2\text{-}3,n}, \ldots, \mathbf{u}_{n_v}, \\ &\quad \mathbf{u}_{n_v,X}, \mathbf{u}_{n_v,Y}\}^{\mathrm{T}},\end{aligned} \tag{51}$$

where $\mathbf{u}_{1-2,n}$ is the degree of freedom denoting the derivative in normal direction at the edge between nodes 1-2 etc.

For the actual generation and implementation of the two elements and the associated stabilizations, the software package *AceGen* [47, 48] was employed. In the following the essential steps and matrices are summarized that are basis of the code derivation.

### 3.2 Consistency part

The projection $\mathbf{u}_\pi$ has now to be inserted into the potential (7) with the strain energy function for large strains (13) and small strains (22). This yields the so called consistency part. Using the general mapping (50), the displacement gradient follows as

$$\nabla\mathbf{u}_\pi = \nabla\mathbb{B}_\beta(\mathbf{X})\,\mathbf{U}_{e\beta}, \tag{52}$$

and its gradient as

$$\nabla\nabla\mathbf{u}_\pi = \nabla\nabla\mathbb{B}_\beta(\mathbf{X})\,\mathbf{U}_{e\beta}\,. \tag{53}$$

Hence the small strain tensor is given within a virtual element $\Omega_e$ by

$$\boldsymbol{\varepsilon}_e = \frac{1}{2}\left\{\nabla\mathbb{B}_\beta(\mathbf{X})\,\mathbf{U}_{e\beta} + \left[\nabla\mathbb{B}_\beta(\mathbf{X})\,\mathbf{U}_{e\beta}\right]^{\mathrm{T}}\right\}, \tag{54}$$

and its gradient by

$$\nabla_X\boldsymbol{\varepsilon}_e = \frac{1}{2}\left\{\nabla\nabla\mathbb{B}_\beta(\mathbf{X})\,\mathbf{U}_{e\beta} + \left[\nabla\nabla\mathbb{B}_\beta(\mathbf{X})\,\mathbf{U}_{e\beta}\right]^{\mathrm{T}}\right\}. \tag{55}$$

For small strains, the potential internal part (4) of (7) yields together with (22) for a virtual element $\Omega_e$:

$$\begin{aligned}U^{\mathrm{lin}}_e(\mathbf{U}_{e\beta}) = \int_{\Omega_e} \Big\{&\frac{\lambda}{2}\left[(\mathrm{tr}\,\boldsymbol{\varepsilon}_e)^2 + l^2\,(\mathbf{1} : \nabla_X\boldsymbol{\varepsilon}_e)\cdot(\mathbf{1} : \nabla_X\boldsymbol{\varepsilon}_e)\right] \\ &+ \mu\,(\boldsymbol{\varepsilon}_e : \boldsymbol{\varepsilon}_e + l^2\nabla_X\boldsymbol{\varepsilon}_e \vdots\cdot \nabla_X\boldsymbol{\varepsilon}_e)\Big\}\,\mathrm{d}\Omega.\end{aligned} \tag{56}$$

In this case, all terms in the integral are polynomials and can be evaluated for an arbitrary polygon exactly as integrals over the element edge since Green's theorem yields

$$\int_{\Omega} x^p y^q \mathrm{d}\Omega = \frac{1}{2} \int_{\Gamma} \left( \frac{x^{p+1} y^q}{p+1} n_x + \frac{x^p y^{q+1}}{q+1} n_y \right) \mathrm{d}\Gamma \,. \tag{57}$$

In case of finite strain elasticity the strain energy, Eq. (13) has to be employed which depends in a nonlinear way on the deformation gradient $\mathbf{F}$ and the strain gradient $\mathbf{G}$. Both kinematic measures can be computed using Eq. (52), which leads to

$$\begin{aligned} \mathbf{F}_e &= \mathbf{1} + \nabla \mathbf{u}_\pi = \mathbf{1} + \nabla \mathbb{B}_\beta(\mathbf{X})\, \mathbf{U}_{e\beta}, \\ \mathbf{G}_e &= \nabla\nabla \mathbf{u}_\pi = \nabla\nabla \mathbb{B}_\beta(\mathbf{X})\, \mathbf{U}_{e\beta}. \end{aligned} \tag{58}$$

The nonlinear strain energies (14) and (16) have to be included in the internal part (4) of the potential (7) leading to

$$\begin{aligned} U_e^{\mathrm{nl}}(\mathbf{U}_{e\beta}) = \int_{\Omega_e} \Big\{ & \frac{\lambda}{4} (J_e^2 - 1 - 2 \ln J_e) \\ & + \frac{\mu}{2} (\mathbf{F}_e : \mathbf{F}_e - 2 - 2 \ln J_e) \\ & + \mu\, l^2\, \mathbf{G} \vdots \mathbf{G} + \frac{\lambda}{2} l^2\, (\mathbf{1} : \mathbf{G}) \cdot (\mathbf{1} : \mathbf{G}) \Big\}\, \mathrm{d}\Omega, \end{aligned} \tag{59}$$

where $J_e = \det \mathbf{F}_e$.

Since this potential is a nonlinear function of the gradients, integration cannot be shifted to the boundary and has to be performed over the element area of $\Omega_e$. By introducing a triangular submesh of each polygonal virtual element, the integration can be carried out using a Gauss point integration [34]. Note that by definition $\mathbf{u}_h$ is not known within the element, and this is overcome by the approximation of $\mathbf{u}_h$ by $\mathbf{u}_\pi$ within the element which can be done without loss of accuracy [49, 50].

A similar argument as above has also to be applied for the evaluation of the external part of the potential (5) which is related to the loading terms. Here we use only the first two parts related to the volume and the surface loads. Insertion of the virtual element ansatz functions yields

$$U_{\mathrm{ext}}(\mathbf{U}_{e\beta}) = -\int_{\Omega} \bar{\mathbf{b}} \cdot \mathbb{B}_\beta(\mathbf{X})\, \mathbf{U}_{e\beta}\, \mathrm{d}\Omega - \int_{\Gamma_N} \bar{\mathbf{t}}^1 \cdot \mathbf{u}_h\, \mathrm{d}\Gamma. \tag{60}$$

The volume load has to be integrated over the element area. For a volume load $\bar{\mathbf{b}}$ with a polynomial form the integral can be shifted to the boundaries. For all other distributions of $\bar{\mathbf{b}}$, the integration has to be performed in the same way as described for Eq. (59). Since $\mathbf{u}_h$ is known at the element edges, the ansatz in Eq. (35) can be applied directly to compute the second integral related to the surface loads.

The residual $\mathbf{R}_e$ and tangent matrix $\mathbf{K}_e$ of the consistency part follows in case of the linear or nonlienar formulation for a virtual element $\Omega_e$ by differentiation of Eqs. (56) or (59) and (60):

$$\mathbf{R}_e = \frac{\partial [U_e^{\mathrm{lin,nl}}(\mathbf{U}_{e\beta}) + U_{\mathrm{ext}}(\mathbf{U}_{e\beta})]}{\partial \mathbf{U}_{e\beta}}, \qquad \mathbf{K}_e = \frac{\partial \mathbf{R}_e(\mathbf{U}_{e\beta})}{\partial \mathbf{U}_{e\beta}}. \tag{61}$$

It is possible to compute the different parts of the tangent matrix that are related to the contribution of displacement gradient $\nabla \mathbf{u}$ and its gradient $\nabla\nabla \mathbf{u}$. These will be denoted by $\mathbf{K}_e^\nabla$ and $\mathbf{K}_e^\Delta$, respectively.

### 3.3 Stabilization

Within the virtual element $\Omega_e$, the strain gradient of the projected part of the displacement $\mathbf{u}$ is approximated by a constant and linear part, depending on the element type, as discussed in the last sections. A virtual element which is based purely on this projection leads clearly to a rank deficient element. Thus the formulation has to be stabilised as it was done for plates in Refs. [38, 41, 51] and in Ref. [44] for the Cahn-Hillard equation. Here we can use basically the same stabilization as discussed in these papers. This leads to a stabilization operator which includes all element nodes (vertices and midpoints):

$$\begin{aligned} &\widehat{U}^e_{\mathrm{stab}}(\mathbf{u}_h - \mathbf{u}_\pi) = \left[ \frac{\mathrm{tr}\mathbf{K}_e^\Delta}{2\, h_e^2} + \frac{\mathrm{tr}\mathbf{K}_e^\nabla}{2} \right] \widehat{S}^e_{\mathrm{stab}}, \\ &\text{with } \widehat{S}^e_{\mathrm{stab}} = \sum_{i=1}^{n_V} \left[ \widehat{\mathbf{u}}(\mathbf{X}_i)^2 + \left\| \frac{L_{i-1} + L_i}{2} \nabla \widehat{\mathbf{u}}(\mathbf{X}_i) \right\|^2 \right. \\ &\qquad \left. + \left\| L_i\, \widehat{\mathbf{u}}_{,n}(\mathbf{X}_i) \right\|^2 \right], \\ &\text{and } \widehat{\mathbf{u}}(\mathbf{X}_i) = \mathbf{u}_h(\mathbf{X}_i) - \mathbf{u}_\pi(\mathbf{X}_i)\,, \\ &\nabla \widehat{\mathbf{u}}(\mathbf{X}_i) = \nabla \mathbf{u}_h(\mathbf{X}_i) - \nabla \mathbf{u}_\pi(\mathbf{X}_i), \\ &\text{and } \widehat{\mathbf{u}}_{,n}(\mathbf{X}_i) = \begin{cases} \mathbf{u}_{h,n}(\mathbf{X}_i) - \mathbf{u}_{\pi,n}(\mathbf{X}_i), & \text{for el 2,} \\ 0, & \text{for el 1.} \end{cases} \end{aligned} \tag{62}$$

Here $h_e$ is the maximum diameter of the virtual element $e$, thus $h_e^2$ can be interpreted as the element area $A_e$. The function $w_h$ and the projection $\Pi(w_h)$ have to be evaluated at the vertices $\mathbf{X}_i$.

The stabilization (62) can be reformulated as an integral describing the total error along the edge instead of using the discrete values. This alternative stabilization takes account of the distribution of each degree of freedom along the edge $\Gamma_k$:

$$\begin{aligned} \widehat{U}^e_{\mathrm{stab}}(\mathbf{u}_h - \mathbf{u}_\pi) = \left[ \frac{\mathrm{tr}\mathbf{K}_e^\Delta}{2\, h_e^2} + \frac{\mathrm{tr}\mathbf{K}_e^\nabla}{2} \right] \sum_{k=1}^{n_E} \frac{1}{L_k} \int_{\Gamma_k} \Big[ & \widehat{\mathbf{u}}(\boldsymbol{X}_k) \cdot \widehat{\mathbf{u}}(\boldsymbol{X}_k) \\ & + \| L_k \nabla \widehat{\mathbf{u}}(\boldsymbol{X}_k) \|^2 \mathrm{d}\Gamma \Big] \,. \end{aligned} \tag{63}$$

Here $A_e$ can be used in this equation instead of $h_e^2$. The edge integral in Eq. (63) is evaluated numerically using Gauss quadrature:

$$\int_{\Gamma_k} f(\boldsymbol{x}_k)\mathrm{d}\Gamma = L_k \sum_{g=1}^{n_g} w_g f(\boldsymbol{x}_g), \tag{64}$$

where for the assumed straight edges the Jacobian $J_\xi$ of the transformation $\mathrm{d}\Gamma = J_\xi \mathrm{d}\xi$ is the length of the $k$th edge $J_\xi = \|\frac{\partial \boldsymbol{X}^\Gamma}{\partial \xi}\| = L_k$ and $\xi \in [0,1]$ is the local coordinate.

When employing stabilization (63) the resulting tangent matrix has full rank. Note that stabilization (62) is easier to implement than the second one in Eq. (63).

## 4. Examples

Several examples will illustrate the general behaviour of the derived $C^1$-continuous virtual elements for gradient elasticity. These cover an investigation of the convergence behaviour using an analytical solution of a small strain problem and the finite strain analysis of a problem with re-entrent corner.

### 4.1 Convergence behaviour of the $C^1$-continuous virtual element

A thick hollow cylinder is subjected to an external pressure as depicted in Fig. 3. The inner radius of the calinder is $R_i = 0.05$ and the outer radius is given by $R_a = 0.5$. The computation is performed using the constitutive equations provided by the strain energy function in Eq. (22). The Làme constants are $\lambda = 7000$ and $\mu = 3000$. The length scale is given as $l = 0.01$. The cylinder is subjected to a pressure load $p = 1.0$. Due to symmetry, only a quarter of the cylinder is discretized using the symmetry conditions $u(X = 0) = 0$ and $v(Y = 0) = 0$, as shown in Fig. 3.

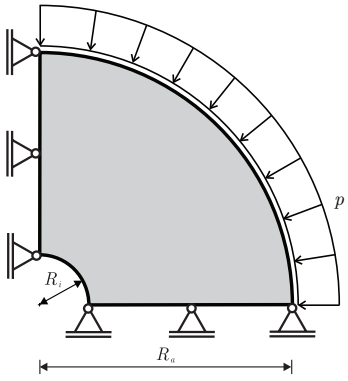


**Figure 3** Geometry and loading of the hollow cylinder.

The mesh is created using the same number of elements in radial and cirumvential direction. The mesh consists of 4 noded (Q1) elements and eight noded (Q2S) elements, as depicted in Fig. 4.

The small strain results can be compared with the analytical solution in Appendix, see also Ref. [22]. Figure 5 reports the convergence results for the prediction of the strains in the hollow cylinder at length scale $l = 0$. Here also comparison of the virtual element discretization can be made with standard finite elements. We note that all element yield basically linear convergence where the virtual element VE2 yields the best results for a mesh consisting of eight noded elements, here called Q2S.

Convergence results for the length scale $l = 0.01$ are depicted in Fig. 6. As expected, we can observe that the VE2 element converges with a higher rate than the VE1 element. We note however that the convergence rate deteriorates for a very fine mesh with more than $10^4$ elements. This is related most probably to the scaling of the stabilization term. A similar behaviour is also reported in Ref. [22] for a $C^1$-element based on a penalty formulation where the solution for finer meshes is influenced by the penalty parameter and thus a detoriation of the convergence rate is visible for the hollow cylinder problem. Since the stabilization in Eqs. (62)

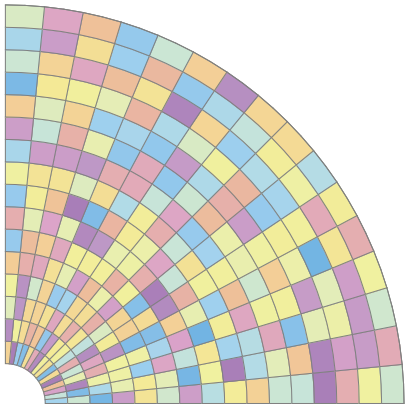

**Figure 4** 16×16 Q2S mesh used for the numerical simulation of the hollow cylinder.

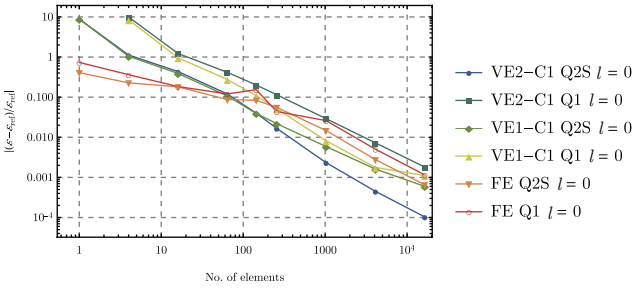


**Figure 5** Convergence study of the strain $\varepsilon_{rr}$ for the hollow cylinder ($l = 0$).

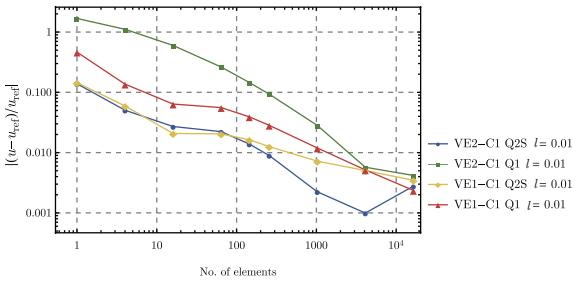


**Figure 6** Convergence study of the displacement $u_r$ for the hollow cylinder ($l = 0.01$).

and (63) acts in a way like a penalization the same behaviour is observed. Here additional research effort is needed to obtain a consistent convergence rate for fine meshes. However for engineering applications the accuracy of the results are more than sufficient.

### 4.2 Small strain response of a L-shaped structure

In the second example, an L-shaped domain is considered, see Fig. 7. This example can be found in Refs. [28,29] where the authors employed different element formulations and the isogeometric analysis to construct $C^1$-continuous discretizations. The domain is loaded at the left side by a constant distributed load $\bar{t} = 100$. The width is given by $W_1 = W_2 = 4$ and the height has the dimension $H_1 = H_2 = 4$. Young's modulus of this problem is $E = 8100$ and the Poisson ratio has the value $\nu = 0.35$.

In Fig. 8, the strain component $\varepsilon_{xy}$ is plotted for different length scales on the deformed configuration which is scaled by a factor of 3. Observe that a very small length scale ($l = 5/2048$) yields a high value of the strains at the re-entrant corner. When compared to a solution with length scale $l = 0$, the strains are almost the same: $\varepsilon_{xy}^{l=0} = 0.05372$ versus $\varepsilon_{xy}^{l=5/2048} = 0.05360$. Hence for very small values of the length scale the gradient effect is negligible. However for larger length scales the influence of the gradient theory is

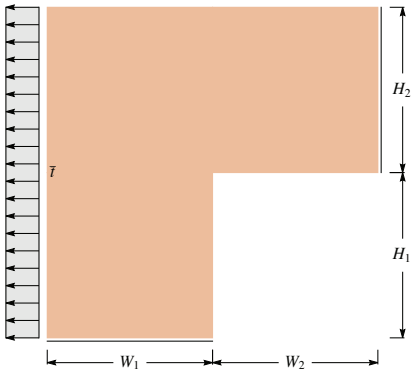


**Figure 7** Geometry and loading of the L-shaped domain.

clearly visible. The stiffness of the solid increases for higher values of the length scale, leading to a smaller deformation, as can be observed in Fig. 8, where the deformed shape of the L-shaped domain is provided. Furthermore, the strain concentration at the re-entrant corner is smeared out due to the gradient effect. This becomes even more obvious for a very high length scales of $l = 5/4$ and $l = 40$ where, in the latter, the structural response is almost rigid. The results are in line with the findings reported in Refs. [28,29].

### 4.3 Large deflection response of a thin arc

The last example illustrates the ability of the new element formulation to compute the highly nonlinear response of thin structures. The deep arc, depicted in Fig. 9 has a radius of $R = 100$. The angle $\alpha$ is set to $\alpha = 17.5^0$. This results in a height $H = 130.07$ and a width $L = 190.74$. The height of the cross section is $h = 3.464$. Young's modulus is $E = 2.887 \cdot 10^5$ and the Poisson ratio is set to $\nu = 0.2$.

The arc is loaded by a single force $F$ in its center and clamped at both ends. Since the response of the deep arc is governed by a snap-through behaviour, the load is applied by a given displacement. Hence the force $F$ is obtained as the reaction force related to the applied displacement.

The load deflection curves are computed for the length scale $l = \frac{\pi R}{4^4}$ of the gradient elastic material given in Eqs. (14) and (18). For comparison with finite element solutions, also a length scale of $l = 0$ is used. The arc is discretized with four and eight noded elements. Four elements are used over the thickness and 64 elements along the length of the arc.

The case $l = 0$ leads to a load deflection curve reported in Fig. 10. It is evident that a Q1 linear finite element locks when applied to solve this problem of a thin arc. Furthermore, it is evident that also the virtual element VE1 with linear approximation of the derivative at the edge is stiffer for both discretizations with 4 and 8 noded virtual elements. The virtual element VE2 which has a consistent approximation of the derivatives results in a converged solution that is also obtained using a Q2S quadratic finite element.

For the case of $l = \frac{\pi R}{4^3}$ and $l = \frac{\pi R}{4^4}$ the force deflection curve in Fig. 11 depicts a much stiffer response of the arc which underlines the stiffening effect due to the strain gradient which was also observed in experimental observation for beams, see Ref. [27]. Especially for the four times larger length scale of $l = \frac{\pi R}{4^3}$ the load deflection curve shows a disproportionate increase of the limit load and clearly the stiffening effect of the gradient term.

The solution, computed with the virtual element VE1, which approximates the strain gradient as a constant, yields a very high limit load which is about 60 % higher than the limit load computed with the VE2 element where the strain gradi-

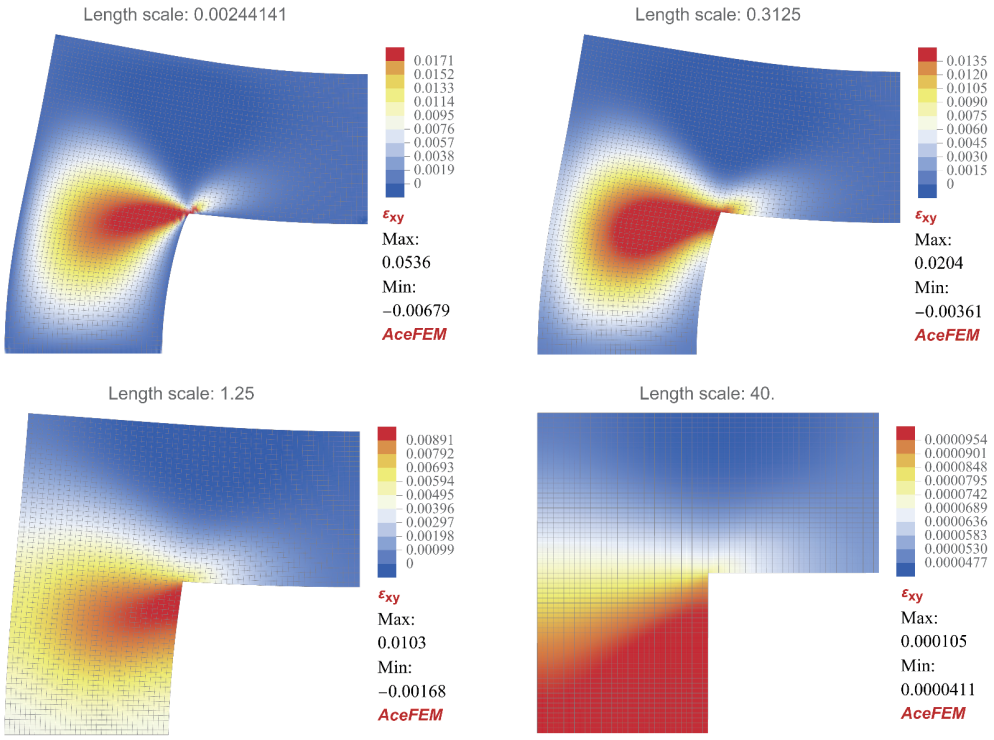


**Figure 8** Strain $\varepsilon_{xy}$ for length scales $l = 5/2048$, $l = 5/16$, $l = 5/4$ and $l = 40$.

ent is approximated by a linear function. Hence for bending situations the virtual element VE2 has to be employed in order to obtain a correct solution, see also Fig. 11. The deformed configuration of the arc is depicted in Fig. 12 for the case of $l = \frac{\pi R}{4^4}$. It is related to the beginning of the snap-through (limit point).

The deformed shape illustrates the large deflection of the arc. It includes the contours of the strains $E_{xx}$ which have their maximum values at the location of the point load.

For a four times larger length scale of $l = \frac{\pi R}{4^3}$, the deformed configuration at the onset of the limit point is depicted in Fig. 13. Again the contours of the strains $E_{xx}$ are included. By comparison with the strain field in Fig. 12, one can see that the strains are now differently distributed, which is due to the length scale effect of the strain gradient elasticity.

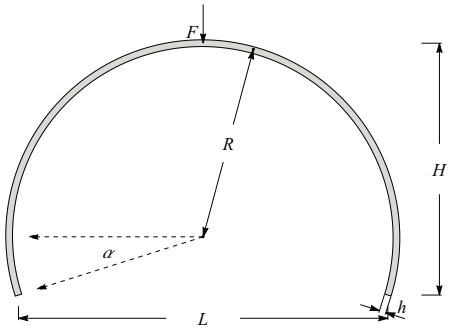


**Figure 9** Geometry and loading of the thin arc.

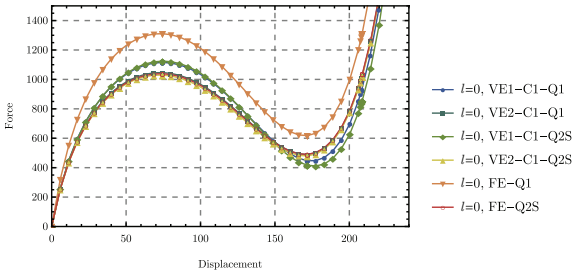


**Figure 10** Load-deflection curve for the arc using the length scale $l = 0$.

## 5. Summary and Conclusions

We have presented a virtual element method for gradient elasticity with respect to small and finite strains. The $C^1$-continuous formulation only used nodal degrees of freedom which are the displacements and its gradients. It could be shown that the method converges well and provides a simple but efficient and robust scheme for higher order continua. As denoted in the examples, the scaling of the stabilization term needs still to be improved. Here eventually also enhanced formulations could be applied as recently discussed in Refs. [52, 53].

The method proposed here is amenable to extensions of

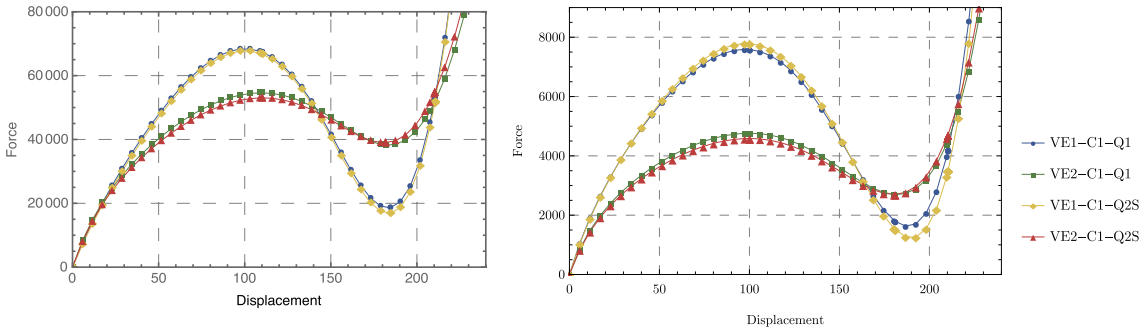


**Figure 11** Load-deflection curves for the arc using the length scales $l = \frac{\pi R}{4^3}$ on the left and $l = \frac{\pi R}{4^4}$ on the right.

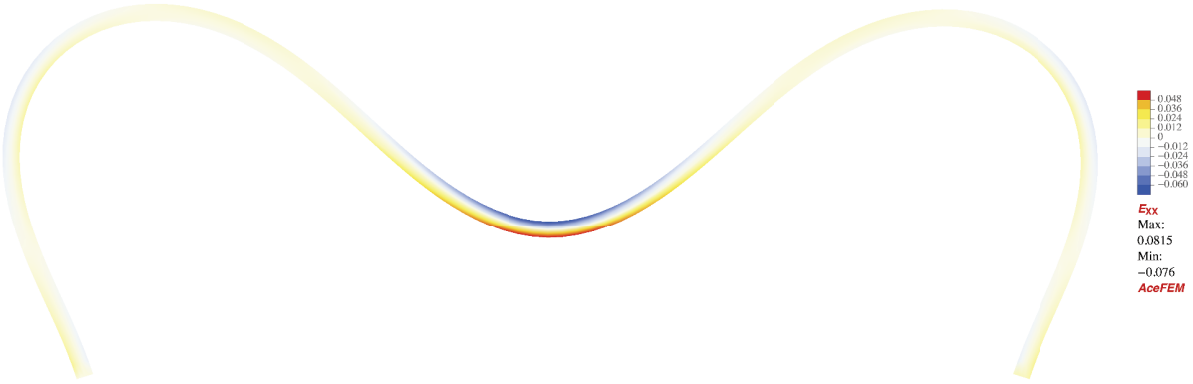


**Figure 12** Deformed shape of the arc for the length scale $l = \frac{\pi R}{4^4}$.

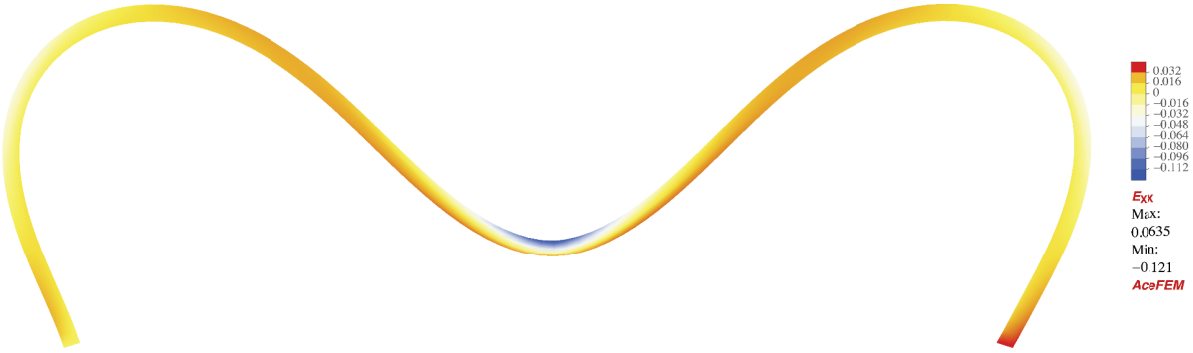


**Figure 13** Deformed shape of the arc for the length scale $l = \frac{\pi R}{4^3}$.

various kinds. Here we mention three dimensional applications, other nonlinear problems involving e.g., inelastic material behaviour or gradient plasticity formulations for crystal plasticity.

***Author contributions*** *Peter Wriggers formulated the overarching research goals and aims, developed the methodology, and created the theoretical models. Peter Wriggers and Blaž Hudobivnik wrote the first draft of the manuscript. Blaž Hudobivnik did the computational work, coded the software related to the research, and performed the numerical simulations. Peter Wriggers and Blaž Hudobivnik revised and edited the final version.*

***Acknowledgements*** *This work was supported by the Deutsche Forschungsgemeinschaft (DFG, German Research Foundation) under Germany's Excellence Strategy within the Cluster of Excellence PhoenixD, EXC 2122 (Grant No. 390833453).*

1 Z. P. Bažant, Size effect, Int. J. Solids Struct. **37**, 69 (2000).
2 N. A. Fleck, G. M. Muller, M. F. Ashby, and J. W. Hutchinson, Strain gradient plasticity: Theory and experiment, Acta Metall. Mater. **42**, 475 (1994).
3 H. T. Zhu, H. M. Zbib, and E. C. Aifantis, Strain gradients and continuum modeling of size effect in metal matrix composites, Acta Mech. **121**, 165 (1997).
4 H. Gao, Mechanism-based strain gradient plasticity? I. Theory, J. Mech. Phys. Solids **47**, 1239 (1999).
5 E. Cosserat, and F. Cosserat, Sur la théorie de l'élasticité. Premier mémoire, Annales de la Faculté des sciences de Toulouse: Mathématiques, 10, I1 (1896).
6 E. Hellinger, Die allgemeinen Ansätze der Mechanik der Kontinua, in: F. Klein and C. Müller, eds. Mechanik (Springer, 1907), pp. 601-694.
7 R. D. Mindlin, and H. F. Tiersten, Effects of couple-stresses in linear elasticity, Arch. Rational Mech. Anal. **11**, 415 (1962).
8 W. Koiter, Couple-stress in the theory of elasticity I, in: Proceedings of the Royal Netherlands Academy of Arts and Sciences (B) (North Holland Pub, 1964a), pp. 17-29.
9 W. Koiter, Couple-stress in the theory of elasticity II, in: Proceedings of the Royal Netherlands Academy of Arts and Sciences (B) (North Holland Pub, 1964b), pp. 30-44.
10 R. A. Toupin, Elastic materials with couple-stresses, Arch. Rational Mech. Anal. **11**, 385 (1962).
11 R. A. Toupin, Theory of elasticity with couple-stress, Arch. Rational Mech. Anal. **17**, 85 (1984).
12 A. C. Eringen, and E. Suhubi, Nonlinear theory of simple micro-elastic solids, Int. J. Eng. Sci. **2**, 189 (1964).
13 R. D. Mindlin, and N. N. Eshel, On first strain-gradient theories in linear elasticity, Int. J. Solids Struct. **4**, 109 (1968).
14 S. B. Altan, and E. C. Aifantis, On the structure of the mode iii crack-tip in gradient elasticity, Scr. Metall. Mater. **26**, 319 (1992).
15 E. C. Aifantis, Strain gradient interpretation of size effects, Int. J. Fract. **95**, 299 (1999).
16 D. C. C. Lam, F. Yang, A. C. M. Chong, J. Wang, and P. Tong, Experiments and theory in strain gradient elasticity, J. Mech. Phys. Solids **51**, 1477 (2003).
17 E. C. Aifantis, On scale invariance in anisotropic plasticity, gradient plasticity and gradient elasticity, Int. J. Eng. Sci. **47**, 1089 (2009).
18 A. Bertram, Finite gradient elasticity and plasticity: A constitutive mechanical framework, Continuum Mech. Thermodyn. **27**, 1039 (2015).
19 A. Beheshti, Generalization of strain-gradient theory to finite elastic deformation for isotropic materials, Continuum Mech. Thermodyn. **29**, 493 (2017).
20 J. Y. Shu, W. E. King, and N. A. Fleck, Finite elements for materials with strain gradient effects, Int. J. Numer. Meth. Eng. **44**, 373 (1999).
21 E. Amanatidou, and N. Aravas, Mixed finite element formulations of strain-gradient elasticity problems, Comput. Methods Appl. Mech. Eng. **191**, 1723 (2002).
22 A. Zervos, S. A. Papanicolopulos, and I. Vardoulakis, Two finite-element discretizations for gradient elasticity, J. Eng. Mech. **135**, 203 (2009).
23 J. C. Reiher, I. Giorgio, and A. Bertram, Finite-element analysis of polyhedra under point and line forces in second-strain gradient elasticity, J. Eng. Mech. **143**, 04016112 (2017).
24 G. Engel, K. Garikipati, T. J. R. Hughes, M. G. Larson, L. Mazzei, and R. L. Taylor, Continuous/discontinuous finite element approximations of fourth-order elliptic problems in structural and continuum mechanics with applications to thin beams and plates, and strain gradient elasticity, Comput. Methods Appl. Mech. Eng. **191**, 3669 (2002).
25 T. Lesičar, Z. Tonković, and J. Sorić, Two-scale computational approach using strain gradient theory at microlevel, Int. J. Mech. Sci. **126**, 67 (2017).
26 S. Papargyri-Beskou, K. G. Tsepoura, D. Polyzos, and D. E. Beskos, Bending and stability analysis of gradient elastic beams, Int. J. Solids Struct. **40**, 385 (2003).
27 N. Challamel, and C. M. Wang, The small length scale effect for a non-local cantilever beam: A paradox solved, Nanotechnology **19**, 345703 (2008).
28 P. Fischer, J. Mergheim, and P. Steinmann, On the $C^1$ continuous discretization of non-linear gradient elasticity: A comparison of NEM and FEM based on Bernstein-Bézier patches, Int. J. Numer. Meth. Eng. **82**, 1282 (2010).
29 P. Fischer, M. Klassen, J. Mergheim, P. Steinmann, and R. Müller, Isogeometric analysis of 2D gradient elasticity, Comput. Mech. **47**, 325 (2011).
30 P. E. Fischer, $C^1$ Continuous Methods in Computational Gradient Elasticity, Dissertation for Doctoral Degree (Friedrich-Alexander-Universitaet Erlangen-Nuernberg, Nuernberg, 2011).
31 L. Beirão da Veiga, F. Brezzi, and L. D. Marini, Virtual elements for linear elasticity problems, SIAM J. Numer. Anal. **51**, 794 (2013).
32 L. Beirão da Veiga, C. Lovadina, and D. Mora, A Virtual Element Method for elastic and inelastic problems on polytope meshes, Comput. Methods Appl. Mech. Eng. **295**, 327 (2015), arXiv: 1503.02042.
33 K. Berbatov, B. S. Lazarov, and A. P. Jivkov, A guide to the finite and virtual element methods for elasticity, Appl. Numer. Math. **169**, 351 (2021).
34 M. L. De Bellis, P. Wriggers, and B. Hudobivnik, Serendipity virtual element formulation for nonlinear elasticity, Comput. Struct. **223**, 106094 (2019).
35 P. Wriggers, M. L. De Bellis, and B. Hudobivnik, A Taylor-Hood type virtual element formulations for large incompressible strains, Comput. Methods Appl. Mech. Eng. **385**, 114021 (2021).
36 F. Aldakheel, B. Hudobivnik, E. Artioli, L. Beirão da Veiga, and P. Wriggers, Curvilinear virtual elements for contact mechanics, Comput. Methods Appl. Mech. Eng. **372**, 113394 (2020).
37 A. Hussein, B. Hudobivnik, and P. Wriggers, A combined adaptive phase field and discrete cutting method for the prediction of crack paths, Comput. Methods Appl. Mech. Eng. **372**, 113329 (2020).
38 F. Brezzi, and L. D. Marini, Virtual element methods for plate bending problems, Comput. Methods Appl. Mech. Eng. **253**, 455 (2013).
39 C. Chinosi, and L. D. Marini, Virtual element method for fourth order problems: L2-estimates, Comput. Math. Appl. **72**, 1959 (2016).
40 D. Mora, and I. Velásquez, Virtual element for the buckling problem of Kirchhoff-Love plates, Comput. Methods Appl. Mech. Eng. **360**, 112687 (2020), arXiv: 1905.02030.
41 P. Wriggers, B. Hudobivnik, and F. Aldakheel, NURBS-based geometries: A mapping approach for virtual serendipity elements, Comput. Methods Appl. Mech. Eng. **378**, 113732 (2021).
42 F. Brezzi, and L. D. Marini, Finite elements and virtual elements on classical meshes, Vietnam J. Math. **49**, 871 (2021).
43 P. Wriggers, On a virtual element formulation for trusses and beams, Arch. Appl. Mech. **92**, 1655 (2022).
44 P. F. Antonietti, L. Beirão da Veiga, S. Scacchi, and M. Verani, A $C^1$ virtual element method for the Cahn-Hilliard equation with polygonal meshes, SIAM J. Numer. Anal. **54**, 34 (2016).
45 P. F. Antonietti, G. Manzini, and M. Verani, The fully nonconforming virtual element method for biharmonic problems, Math. Model.

Methods Appl. Sci. **28**, 387 (2018).
46 P. Wriggers, B. Hudobivnik, and O. Allix, On two simple virtual Kirchhoff-Love plate elements for isotropic and anisotropic materials, Comput. Mech. **69**, 615 (2022).
47 J. Korelc, Automatic generation of numerical codes with introduction to AceGen 4.0 symbolc code generator, http://www.fgg.uni-lj.si/Symech (2000).
48 J. Korelc, and P. Wriggers, Automation of Finite Element Methods (Springer, Berlin, 2016).
49 B. Ahmad, A. Alsaedi, F. Brezzi, L. D. Marini, and A. Russo, Equivalent projectors for virtual element methods, Comput. Math. Appl. **66**, 376 (2013).
50 L. Beirão da Veiga, F. Brezzi, L. D. Marini, and A. Russo, The Hitchhiker's guide to the virtual element method, Math. Model. Methods Appl. Sci. **24**, 1541 (2014).
51 D. Mora, G. Rivera, and I. Velásquez, A virtual element method for the vibration problem of Kirchhoff plates, ESAIM-M2AN **52**, 1437 (2018).
52 A. M. D'Altri, S. de Miranda, L. Patruno, and E. Sacco, An enhanced VEM formulation for plane elasticity, Comput. Methods Appl. Mech. Eng. **376**, 113663 (2021), arXiv: 2101.05548.
53 A. Chen, and N. Sukumar, Stabilization-free virtual element method for plane elasticity, arXiv: 2202.10037.

# 梯度弹性的虚拟单元公式

Peter Wriggers, Blaž Hudobivnik

**摘要** 虚拟单元法在过去十年中得到了发展, 并应用于固体力学中的问题. 目前已使用了不同的公式来解释该方法的顺序和稳定性, 并应用到包括弹性和非弹性材料以及压裂过程的多种问题中. 本文利用虚拟单元法固有的可能性, 以简单有效的方式, 建立$C^1$连续的弹性函数, 研究固体高梯度弹性理论的虚拟单元公式.